CrossMark

JM PAPERS

Quadrupole noise generated from a low-speed aerofoil in near- and full-stall conditions

Jacob M. Turner[1],† **and Jae Wook Kim**[1]

[1]Institute of Sound & Vibration Research, University of Southampton, Southampton SO17 1BJ, UK

In this paper, direct numerical simulations are performed for low-speed flows past a NACA0012 aerofoil at high incidence angles. The aim is to investigate the significance of quadrupole noise generated due to separated shear layers, in comparison to dipole noise emanating from the aerofoil surface. The two different noise components (dipole and quadrupole) are calculated by using the Ffowcs Williams & Hawkings method in two different approaches: one with a solid surface and another with a permeable surface. The quadrupole noise is then estimated approximately by taking the relative difference between the two. The current study provides detailed comparisons between the quadrupole and dipole noise components at various observer locations in a wide range of frequencies. The comparisons are also made in terms of Mach number scaling, which differs significantly from theoretical predictions and changes rapidly with frequency. Additionally, pre-, near- and full-stall conditions are cross-examined, which reveals significant differences in the quadrupole contributions, including changes in the major source locations and frequencies. It is found that the inclusion of the quadrupole sources gives rise to the predicted noise power level at all frequencies (varying between 2 and 10 dB for an observer above the aerofoil) compared to the dipole-only case. The quadrupole contribution is far from negligible even at the low subsonic speeds (Mach 0.3 and 0.4) when aerofoil stall occurs.

Key words: aeroacoustics, separated flows

1. Introduction

Studies on aerofoil trailing edge (TE) noise generated by a turbulent boundary layer scattered at the TE have been well established since the 1970s. For low incidence angles in the absence of inflow disturbances, TE noise is usually considered the main part of aerofoil self-noise. However, in many engineering applications, aerofoils often operate at higher incidence angles than is ideal, and encounter varying degrees of flow separation. In an extreme event, aerofoils may enter a stalled condition where the noise generation no

† Email address for correspondence: j.m.turner@soton.ac.uk

936 A34-1

possible contribution from quadrupole sources. This has received virtually no attention since Wolf *et al.* (2012), mainly due to studies limited to very low Mach numbers. Therefore providing some useful insight into the role of quadrupole sources for separated or stalled flow conditions is the motivation of this paper. For this, direct numerical simulations are carried out for a NACA0012 aerofoil at $Re_\infty = 50\,000$ in three different (pre-, near- and full-stall) flow conditions. Additionally, two different Mach numbers (0.3 and 0.4) are investigated for the full-stall case. Two different approaches are used: solid- and permeable-surface integrations are implemented for the Ffowcs Williams & Hawkings (FWH) acoustic calculation. First, the quadrupole contributions are quantified relative to the dipole counterpart. Second, a discussion is given on the Mach number scaling between the quadrupole and dipole components. Finally, differences between the pre-, near- and full-stall cases are examined and related to the changes in the quadrupole noise characteristics.

The paper is organised into the following parts. Section 2 presents the current computational set-up, including the acoustics calculation based on FWH. In § 3, the FWH method is discussed, including a sensitivity test of the permeable approach. Section 4 compares the calculated far-field sound obtained through both solid and permeable FWH integration methods for the full-stall case. Section 5 considers the influence of Mach number. In § 6, the effect of angle of attack is investigated. Finally, in § 7, overall conclusions are provided and possible future work is discussed.

2. Computational setup

In this paper, we consider a NACA0012 aerofoil with a sharp TE at Reynolds number 50 000. Two different free-stream Mach numbers (0.3 and 0.4) and three incidence angles (5°, 10° and 15°) are explored. Under the current flow conditions, the aerofoil experiences a leading edge (LE) stall process as the angle of attack is increased, caused by laminar boundary layer separation. The pre-stall condition is an example of a classical laminar separation bubble. As the incidence angle is increased, the bubble is shifted towards the LE, eventually bursting due to an excessive adverse pressure gradient. In full-stall, the flow is characterised by instabilities such as Kelvin–Helmholtz vortex shedding in the separated shear layer (SSL), which develops into a von Kármán vortex street downstream of the TE. The instantaneous flow and sound fields are visualised for the stalled case in figure 1 by iso-surfaces of streamwise vorticity (ω_x) coloured by streamwise velocity magnitude, and divergence of velocity contours ($\nabla \cdot \boldsymbol{u}$), respectively.

2.1. *Governing equations and numerical methods*

A conservative form of the three-dimensional compressible Navier–Stokes equations written in a generalised coordinate system is used for the current direct numerical simulation (DNS):

$$\frac{\partial}{\partial t}\left(\frac{\boldsymbol{Q}}{J}\right) + \frac{\partial}{\partial \xi_i}\left(\frac{\boldsymbol{E}_j - Re_\infty^{-1}M_\infty \boldsymbol{F}_j}{J}\frac{\partial \xi_i}{\partial x_j}\right) = -\frac{a_\infty}{L_c}\frac{\boldsymbol{S}}{J}, \qquad (2.1)$$

where the indices $i = 1, 2, 3$ and $j = 1, 2, 3$ denote the three dimensions, and a_∞ is the ambient speed of sound. The vectors of the conservative variables, inviscid and viscous
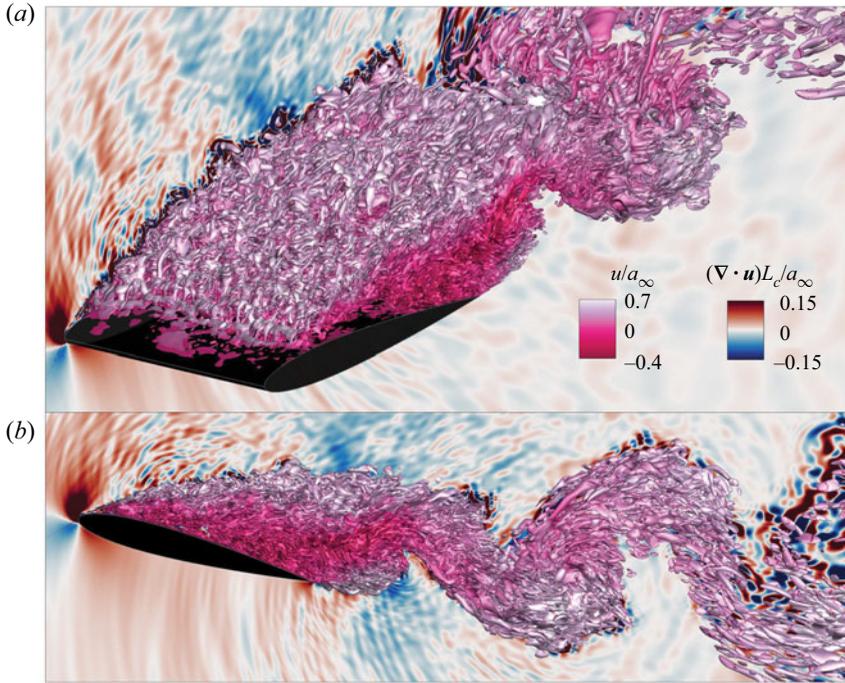
Figure 1. Snapshot of streamwise vorticity iso-surfaces ($\omega_x L_c/a_\infty = \pm 8$) coloured by streamwise velocity (normalised). Dilatation $(\nabla \cdot \boldsymbol{u})L_c/a_\infty$ contours are shown in the xy-plane at $z = -0.5L_c$. (*a*) Isometric view; (*b*) side view.

fluxes, are given by

$$\left.\begin{aligned}
\boldsymbol{Q} &= [\rho, \rho u, \rho v, \rho w, \rho e_t]^{\mathrm{T}}, \\
\boldsymbol{E}_j &= [\rho u_j, (\rho u u_j + \delta_{1j}p), (\rho v u_j + \delta_{2j}p), (\rho w u_j + \delta_{3j}p), (\rho e_t + p)u_j]^{\mathrm{T}}, \\
\boldsymbol{F}_j &= [0, \tau_{1j}, \tau_{2j}, \tau_{3j}, u_i\tau_{ji} + q_j]^{\mathrm{T}},
\end{aligned}\right\} \quad (2.2)$$

with the stress tensor and heat flux vector written as

$$\tau_{ij} = \mu\left(\frac{\partial u_i}{\partial x_j} + \frac{\partial u_j}{\partial x_i} - \frac{2}{3}\delta_{ij}\frac{\partial u_i}{\partial x_i}\right), \quad q_j = \frac{\mu}{(\gamma - 1)Pr}\frac{\partial T}{\partial x_j}, \quad (2.3a,b)$$

where $\xi_i = \{\xi, \eta, \zeta\}$ are the generalised coordinates, $x_j = \{x, y, z\}$ are the Cartesian coordinates, δ_{ij} is the Kronecker delta, $u_j = \{u, v, w\}$, $e_t = p/[(\gamma - 1)\rho] + u_ju_j/2$, and $\gamma = 1.4$ for air. The local dynamic viscosity μ is calculated by using Sutherland's law (White 1991). In the current set-up, ξ, η and ζ are aligned in the streamwise, vertical and lateral directions, respectively. The Jacobian determinant of the coordinate transformation (from Cartesian to generalised) is given by $J^{-1} = |\partial(x, y, z)/\partial(\xi, \eta, \zeta)|$ (Kim & Morris 2002). The extra source term $\boldsymbol{S}$ on the right-hand side of (2.1) is non-zero within the sponge layer only, which is described in Kim, Lau & Sandham (2010*a,b*). In this paper, the free-stream Mach and Reynolds numbers are defined as $M_\infty = u_\infty/a_\infty$ and $Re_\infty = \rho_\infty u_\infty L_c/\mu_\infty$. The governing equations are non-dimensionalised based on the aerofoil chord length L_c for length scales, the ambient speed of sound a_∞ for velocities, L_c/a_∞ for time scales, and $\rho_\infty a_\infty^2$ for pressure. Temperature, density and dynamic viscosity are normalised by their respective ambient values: T_∞, ρ_∞ and μ_∞.

The governing equations given above are solved by using high-order accurate numerical methods developed specifically for aeroacoustic simulations on structured grids. The flux derivatives in space are calculated based on fourth-order pentadiagonal compact finite difference schemes with seven-point stencils (Kim 2007). Explicit time advancing of the numerical solution is carried out by using the classical fourth-order Runge–Kutta scheme with Courant–Friedrichs–Lewy (CFL) number 1.0. Numerical stability is maintained by implementing sixth-order pentadiagonal compact filters for which the cutoff wavenumber (normalised by the grid spacing) is set to 0.8π in interior regions and ramped up to π at the boundaries (Kim 2010). In addition to the sponge layers used, characteristics-based non-reflecting boundary conditions (Kim & Lee 2000) are applied at the far boundaries in order to prevent any outgoing waves from returning to the computational domain. Periodic conditions are used across the spanwise boundary planes as indicated earlier. On the aerofoil surface, no-slip wall boundary conditions are implemented (Kim & Lee 2004).

A moving frame technique is used to initialise the simulations, which gradually ramps the velocity from zero to the free-stream value $(u_\infty, v_\infty, w_\infty) = (|\boldsymbol{u}|\cos(\alpha), |\boldsymbol{u}|\sin(\alpha), 0)$. Each simulation is run for a total of $T^* = t\,a_\infty/L_c = 200$ non-dimensional time units. The approximate time step size (provided by the CFL number) is $\Delta t\,a_\infty/L_c = 1 \times 10^{-4}$. Data are collected during the final 20 non-dimensional time units for post-processing of the acoustics signals. The spectra in this paper are presented based on either one-third or one-twelfth octave averaging. The sensitivity of the results to the time series length is tested in the Appendix.

2.2. *Computational domain and grid*

The computational domain is a rectangular cuboid with the aerofoil at the centre. The outer boundaries of the *xy*-plane (where *x* and *y* are the horizontal and vertical coordinates, respectively) are surrounded by a sponge layer through which numerical reflections are attenuated. The entire computational domain, the inner region (physical domain) where meaningful simulation data are obtained, and the sponge layer zone are defined as

$$\left.\begin{aligned}
\mathcal{D}_\infty &= \{\boldsymbol{x} \mid x/L_c \in [-9, 9], y/L_c \in [-9, 9], z/L_z \in [-1/2, 1/2]\}, \\
\mathcal{D}_{phys} &= \{\boldsymbol{x} \mid x/L_c \in [-7, 7], y/L_c \in [-7, 7], z/L_z \in [-1/2, 1/2]\}, \\
\mathcal{D}_{sponge} &= \mathcal{D}_\infty - \mathcal{D}_{phys},
\end{aligned}\right\} \tag{2.4}$$

where L_z is the spanwise domain length. The aerofoil's leading and trailing edges are located at $x/L_c = -1/2$ and $1/2$, respectively. The default spanwise domain size is one chord length ($L_z = L_c$), unless stated otherwise. This is considered to be sufficient for reliable simulations in stall conditions. A numerical validation on this has been undertaken previously by the authors (Turner & Kim 2020*b*).

The current numerical simulations are performed on a structured H-topology grid that is stretched in both the horizontal and vertical directions (uniform in span), with the smallest cells positioned on the aerofoil surface. Additional refinement is implemented in the wake region of the aerofoil, specifically the first two chord lengths above the aerofoil, which corresponds roughly to the wake height at the domain outlet, and the first two chord lengths downstream of the TE. A total of $(N_\xi, N_\eta, N_\zeta) = (1200, 1120, 326)$ grid cells are used in the three respective directions, distributed over 6720 processor cores on ARCHER. The full domain and grid with the aerofoil at the centre is shown in figure 2(*a*), with one in five points plotted. The grid lines are coloured by the streamwise component of velocity, which demonstrates the asymmetric distribution of points between
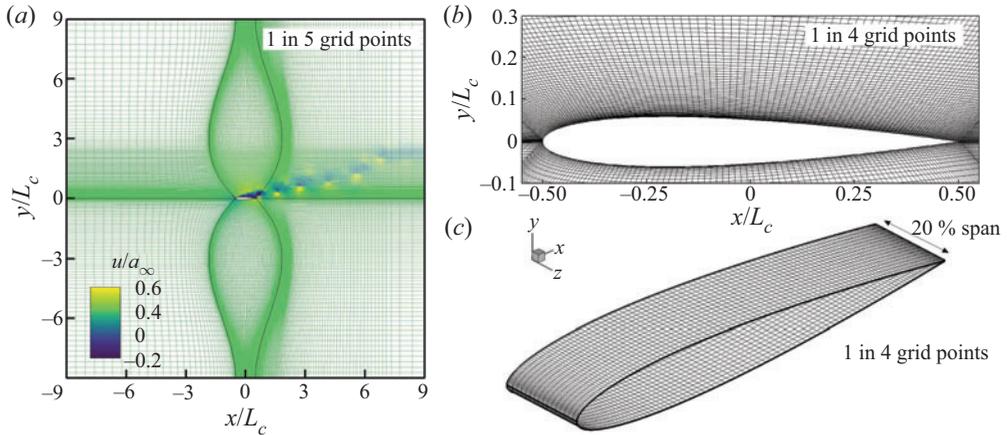
Figure 2. Computational mesh used in the numerical set-up. (*a*) Side view of full domain with grid lines coloured by streamwise velocity u/a_∞ (every fifth point shown in each direction). (*b*) Close-up of NACA0012 profile (every fourth point shown in each direction). (*c*) Aerofoil surface mesh (every fourth point shown in each direction).
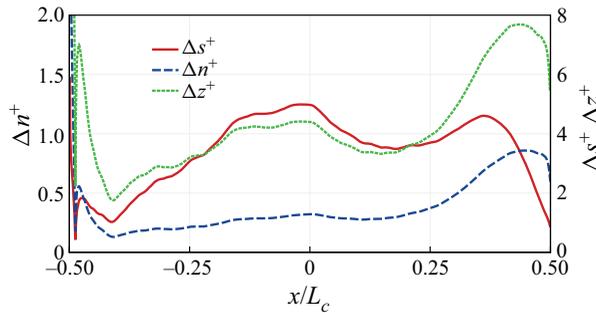
Figure 3. Time- and spanwise-averaged grid sizes in wall units over the aerofoil surface. Δs and Δn represent the body-fitted and wall-normal spacings, respectively.

the upper and lower half-planes. At the current Reynolds number, the aerofoil pressure side remains laminar and therefore requires less grid resolution than the suction side, where transition and separation occur. Additionally, in figure 2(*b,c*) a side view close-up near the aerofoil and the surface mesh are shown with one in four points plotted. The spanwise- and time-averaged surface mesh sizes in wall units are shown in figure 3. Approximate requirements for DNS mesh sizes have been suggested by Georgiadis, Rizzetta & Fureby (2010) as $10 \le \Delta x^+ \le 20$, $\Delta y^+ < 1$ and $5 \le \Delta z^+ \le 10$. The current mesh sizes remain either within or below these requirements over the full aerofoil surface. An extensive validation of the current numerical set-up has been carried out in Turner & Kim (2020*b*), including verification of the spanwise domain size and comparison to experiments for aerodynamic coefficients. In addition, the wall mesh sizes away from the wall have been compared in the previous paper to the local Kolmogorov micro-scale $\eta = (\nu^3/\epsilon)^{1/4}$. It was found that the turbulent regions mostly satisfy $J^{1/3} < 4\eta$, with a maximum value around 5.5η. Additionally, a grid refinement study for the far-field noise prediction is included in the Appendix.

936 A34-6

The computation is parallelised via domain decomposition and message passing interface (MPI) approaches. The compact finite difference schemes and filters used are implicit in space due to the inversion of pentadiagonal matrices involved, which requires a precise and efficient technique for the parallelisation in order to avoid numerical artefacts that may appear at the subdomain boundaries. A parallelisation approach based on quasi-disjoint matrix systems (Kim 2013) offering super-linear scalability is used in the present paper.

2.3. *Definition of variables for statistical analysis*

Data processing and analysis are carried out upon the completion of each simulation. The far-field (acoustic) pressure is defined as

$$p_a(\boldsymbol{x}, t) = p(\boldsymbol{x}, t) - \bar{p}(\boldsymbol{x}), \tag{2.5}$$

where $\bar{p}(\boldsymbol{x})$ is the time-averaged pressure. Following the definitions used in Goldstein (1976), the Fourier transform of p_a can then be calculated as

$$P_a(\boldsymbol{x}, f, T) = \int_{-T}^{T} p_a(\boldsymbol{x}, t) \, e^{2\pi i f t} \, dt, \tag{2.6}$$

and the one-sided frequency-based power spectral density (PSD) function as

$$S_{ppa}(\boldsymbol{x}, f) = \lim_{T \to \infty} \frac{P_a(\boldsymbol{x}, f, T) \, P_a^*(\boldsymbol{x}, f, T)}{T}, \tag{2.7}$$

where '$*$' denotes a complex conjugate. The same definitions can also be used to calculate the spectra of other variables. The sound power spectra are calculated by integrating the fluctuating pressure PSD between two observer angles θ_1 and θ_2:

$$W(\theta_1, \theta_2, f) = \frac{Rb}{\rho_\infty a_\infty} \int_{\theta_1}^{\theta_2} S_{ppa}(\theta, f) \, d\theta, \tag{2.8}$$

where $R = 10L_c$ is the distance from the aerofoil mid-chord to the observers, and b is the span of the integration surface, taken as $25L_c$ for consistency with the FWH calculations. For the majority of the spectra presented in this paper, $\theta_2 - \theta_1 = 20°$, and θ_0 is the middle observer angle. We also define two normalised frequencies used throughout the paper:

$$\left.\begin{aligned} St_u &= fL_c/u_\infty, \\ St_a &= fL_c/a_\infty. \end{aligned}\right\} \tag{2.9}$$

3. Far-field extrapolation approach

In this paper, the far-field noise is calculated by using the FWH method (Ffowcs Williams & Hawkings 1969) based on two different approaches: (1) solid wall, and (2) permeable surface integrations. Theoretically, a permeable integration surface is capable of capturing both surface dipoles and volume quadrupoles (if it surrounds all the turbulence). This kind of approach is often preferable over calculating directly volume quadrupole terms due to the excessive cost (in terms of both time and memory) required. One of the first

permeable-surface-based FWH formulations is the time domain solution proposed by Di Francescantonio (1997), which is used in the current study:

$$
4\pi \, p_P(\boldsymbol{x}, t) = \int \left[\frac{\rho_\infty \dot{U}_i n_i}{r|1 - M_r|^2} + \frac{\rho_\infty U_i n_i a_\infty (M_r - M^2)}{r|1 - M_r|^3} \right]_{ret} \mathrm{d}S_P
$$
$$
+ \int \left[\frac{\dot{F}_i \hat{r}_i}{a_\infty r|1 - M_r|^2} + \frac{\dot{F}_i \hat{r}_i - F_i M_i}{r^2|1 - M_r|^2} + \frac{F_i \hat{r}_i (M_r - M^2)}{r^2|1 - M_r|^3} \right]_{ret} \mathrm{d}S_P \quad (3.1)
$$

and

$$
F_i = L_{ij} n_j, \quad U_i = u_i + [(\rho/\rho_\infty - 1)](u_i - v_i), \quad L_{ij} = p'\delta_{ij} + \rho u_i(u_j - v_j), \quad (3.2a\text{--}c)
$$

where v_i is the surface velocity, n_j is the surface normal, and δ_{ij} is the Kronecker delta. Dotted variables indicate the time derivative, while subscript *ret* indicates that variables are analysed at the retarded time $\tau = t - r/a_\infty$. The above integration is performed on the permeable surface S_P that encloses the aerofoil and full wake. For problems involving rectilinear motion, the retarded time can be determined uniquely via the Garrick triangle (Garrick & Watkins 1953), extended below for two-dimensional mean flow velocity:

$$
r = \frac{M_1 d_1 + M_2 d_2 + \sqrt{(M_1 d_1 + M_2 d_2)^2 + (1 - M_1^2 - M_2^2)[d_1^2 + d_2^2 + d_3^2]}}{1 - M_1^2 - M_2^2}, \quad (3.3)
$$

where $M_i = v_i/a_\infty$ and $d_i = (x_o - x_s, y_o - y_s, z_o - z_s)$, with subscripts o and s representing observer and source, respectively. Additionally, $M_r = \boldsymbol{M} \cdot \hat{\boldsymbol{r}}$, where $\boldsymbol{r}$ is the radiation vector, and $\hat{\ }$ indicates a unit length.

Meanwhile, a second FWH calculation is performed by using a solid-surface integration on the aerofoil. Equation (3.1) is simplified considerably by noting that $u_i = v_i$ due to the no-slip condition. This returns the well-known formulation 1A proposed by Farassat & Succi (1980):

$$
4\pi \, p_S(\boldsymbol{x}, t) = \int \left[\frac{\dot{p}' n_i \hat{r}_i}{a_\infty r|1 - M_r|^2} + \frac{p' n_i \hat{r}_i - p' M_i n_i}{r^2|1 - M_r|^2} \right]_{ret} \mathrm{d}S_S
$$
$$
+ \int \left[\frac{(M_r - M^2)p' n_i \hat{r}_i}{r^2|1 - M_r|^3} + \frac{\rho_\infty a_\infty v_i n_i (M_r - M^2)}{r^2|1 - M_r|^3} \right]_{ret} \mathrm{d}S_S. \quad (3.4)
$$

From here on, we refer to (3.4) and (3.1) as the FWH-S and FWH-P solutions, respectively. As mentioned earlier, the FWH-P solution is expected to contain all noise components in full. However, the FWH-S solution consists mainly of the dipole noise and partially of the secondary quadrupole noise scattered by the aerofoil body. If we focus on the primary dipole component of the FWH-S solution, then the following approximations could be used:

$$
\left.\begin{array}{c}
p_{Total} = p_P, \\
p_D \simeq p_S, \\
p_Q \simeq p_P - p_S.
\end{array}\right\} \quad (3.5)
$$

It is important to also account for the spanwise periodic boundary condition present in the numerical simulations within the FWH integration. This is essential to obtain the same radiated sound amplitude as signal probes positioned in the grid. This can be accomplished by performing repeated surface integrations on spanwise-shifted domains

936 A34-8

until a converged result is obtained. Despite the aerofoil being effectively infinite in span, convergence occurs due to r increasing and $n_i \hat{r}_i \rightarrow 0$ as the z coordinate increases relative to the observer. For the current problem, 25 spanwise domain lengths (25 chords) were required to reach convergence.

The computational cost saving offered by the permeable approach (compared to volume integration) is especially useful for the current DNS cases, which produce large datasets of size ~ 10 TB. Despite this clear advantage, there are some practical considerations required to ensure reliable results. Strictly speaking, the surface must surround the entire turbulent region for the quadrupole sound to correctly determined. Additionally, the surface should be placed in a region of adequate grid resolution to capture the desired acoustic wavelengths. Often these restrictions are not practical. It is a fairly common practice to truncate the surface in the downstream direction – usually, to reduce the computation cost or due to excessive downstream grid stretching. For problems with large wakes or jets, surface truncation can result in the hydrodynamic perturbations perpendicularly crossing the surface end-plane. In doing this, the fluid perturbations manifest as an unphysical noise source in the FWH equations. Several treatments have been proposed to minimise end-plane errors. One of the simplest is to use an 'open surface', where the end-cap is ignored during integration. This has the obvious drawback of missing some of the acoustic information, mainly for observers directly downstream. Another common technique is to employ additional averaged end-caps (Shur, Spalart & Strelets 2005). This method aims to force phase interference in the time signals of the convected disturbances due to the different retarded times on each end-plane. Although this approach can be effective, it is not exact, and there is a danger of choosing the end-plane locations arbitrarily if the results are not compared against experimental data. Additionally, the effectiveness of the averaging approach relies on a contrast between the convection speeds of the turbulence and the sound. At $M_\infty = 0.4$ this could pose a problem for sound waves convecting against the mean flow. Experimental acoustic data for stalled aerofoils is scarce, especially under the current flow conditions. Consequently, we prefer to minimise additional treatments where possible, opting to contain as much of the wake as possible within the surface (rather than truncating).

Four surfaces shown in figure 4 are tested to verify the consistency of the results. The first surface (S1) is a tight-fit truncated surface, avoiding the coarse grids in the downstream sponge region. Comparatively, S2 extends the full length of the computational domain. Both open and closed variants of S2 are considered. S3 and S4 are full-length surfaces with increasing vertical offset from the wake. Figure 5 shows the far-field data predicted with the four integration surfaces. The normalised sound power is shown for $\theta_0 = 90°$ in figure 5(a), while directivity plots are shown for $St_u = 0.75$, 3.0 and 12.0 in figures 5(b–d). All four surfaces obtain comparable results for spectra and directivity at mid-to-high frequencies $St_u > 3.0$. At lower frequency, the S2 closed surface shows significant differences from the others despite the end-plane position at the domain exit. Most notably, it incorrectly predicts the von Kármán shedding frequency $St_u = 0.75$, which is known from previous work (Turner & Kim 2020a). A consistent result is obtained by the surfaces S3 and S4 at all frequencies, which demonstrates convergence of the top and bottom surface boundary locations. The open S1 and S2 results are also comparable to S3 and S4, except for directly upstream at $St_u = 0.75$ and downstream at $St_u = 3.0$. The downstream lobes predicted by S1 and S2 at $St_u = 3.0$ are suspect since the surface end-plane is open. Additionally, the lobes are gradually reduced by loosening the vertical surface boundaries.

The four surfaces are also tested by comparing with a direct noise computation obtained by a probe positioned at $\boldsymbol{x}_o = (0, 3L_c, 0)$. The resulting spectra are shown in figure 6.
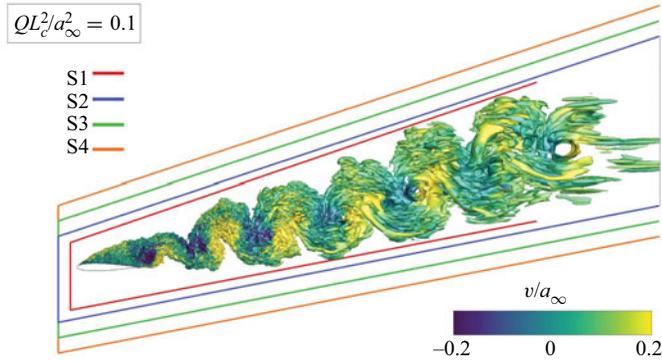
Figure 4. FWH integration surfaces (S1–S4) shown alongside the unsteady flow field. The aerofoil wake is visualised by iso-surfaces of normalised Q-criterion (QL_c^2/a_∞^2) coloured by vertical velocity.
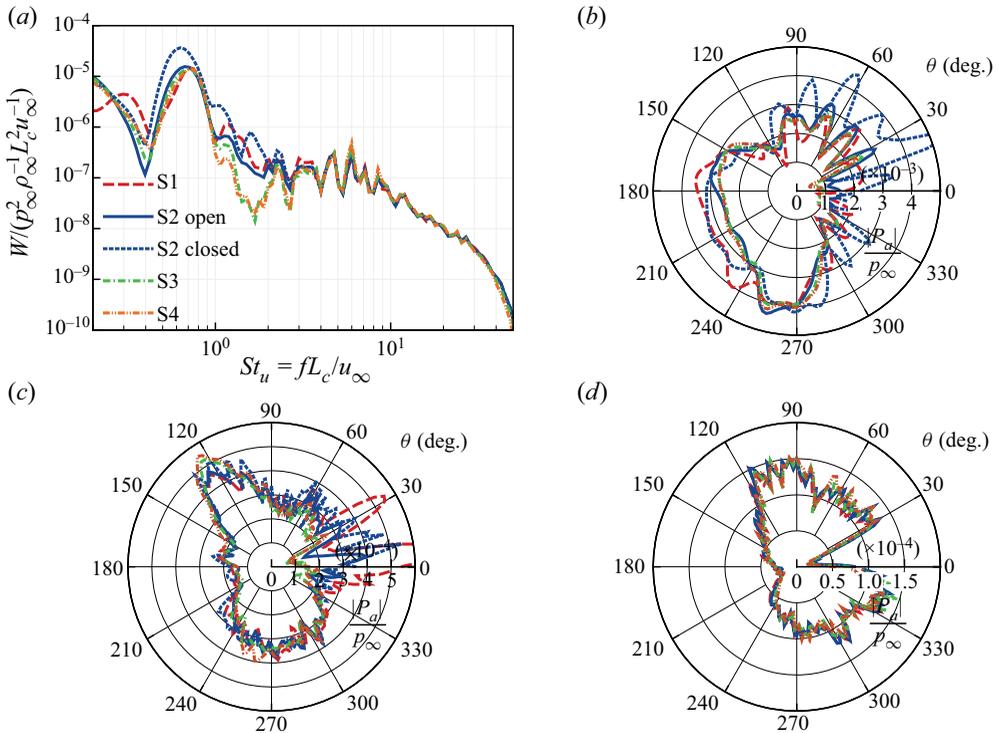
Figure 5. Far-field noise predictions obtained with the four FWH integration surfaces (see figure 4). (*a*) One-twelfth octave averaged normalised sound power for $\theta_0 = 90°$. One-third octave averaged sound directivity plots based on the magnitude of acoustic pressure Fourier transform at $R = 10L_c$ for (*b*) $St_u = 0.75$, (*c*) $St_u = 3.00$, and (*d*) $St_u = 12.00$.

The best agreement is obtained by using either surface S3 or surface S4. The only exception is for very high frequencies ($St_u > 20$), where the probe solution begins to suffer from dissipation due to grid stretching. The result demonstrates that ignoring the end-cap data does not significantly impact the accuracy of the FWH prediction if the surface is carefully selected (and extends the full length of the wake). Consequently, the S4 surface is used for the calculations carried out in this paper.

Figure 6. PSD of acoustic pressure (one-twelfth octave averaged) obtained by a probe at $x_o = (0, 3L_c, 0)$. Comparison is made with the FWH-P predictions based on the surfaces (*a*) S1, S2, and S2 closed, and (*b*) S3 and S4.

4. Significance of quadrupole noise contributions

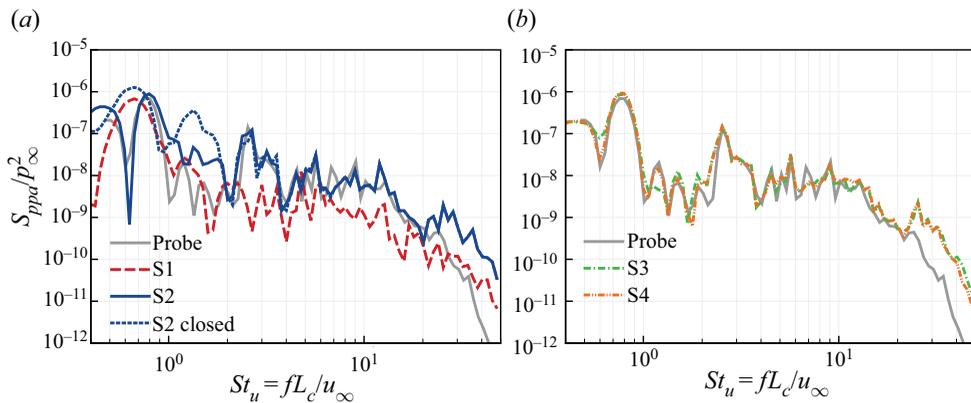In previous work by the authors, the dipole noise was investigated under the same flow conditions (Turner & Kim 2020*a*). Although it was not the focus of the previous study, there was convincing evidence of significant quadrupole sources, particularly for near- and full-stall conditions. The divergence of velocity contours shown in figure 1 indicates how noise radiates from the SSL close to the LE. Furthermore, sound waves are radiated from the vortex roll-ups in the wake seen in figure 1(*b*). This is in contrast to a typical dipole sound field expected for low angles of incidence, radiated primarily from the TE.

The far-field sounds predicted by the FWH-S and FWH-P approaches are compared in this section to determine approximately the increase in total noise due to quadrupole sources. The PSD functions of acoustic pressure predicted by the two approaches are shown in figure 7(*a,b*) for observer angles $\theta = 90°$ and 270°. At $\theta = 90°$, increased noise amplitude is predicted by the FWH-P approach for most of the frequency range. Most notably, in the range $4 \leq St_u \leq 30$, the increase is approximately 10 dB or more, indicating that the quadrupole contribution is dominant. This differs from the aerofoil underside, $\theta = 270°$, where the two solutions are more comparable except for at low frequencies. The difference between the radiated noise above and below the aerofoil is due to two reasons. First, there should be some sound blockage due to the turbulent flow appearing on only the aerofoil suction side, resulting in higher quadrupole levels above the aerofoil. This should affect sound waves generated by the SSL more severely than those from large structures in the wake, possibly explaining why an increase is observed for low frequencies at $\theta = 270°$. Second, the dipole noise is biased towards the lower half-plane due to the positive incidence angle. This can be explained by considering the Doppler factor term $|1 - M_r|^2$ appearing in the leading term of (3.4), which differs by approximately a factor of 1.5 between the upper and lower half-planes.

Third octave band directivity plots are shown in figures 8(*a–f*) based on the magnitude of acoustic pressure Fourier transform at six Strouhal numbers: $St_u = 0.75$, 1.5, 3.0, 6.0, 12.0 and 24.0. In addition to the FWH-S (p_D) and FWH-P (p_{Total}) solutions, the Fourier transform of p_Q is also included. At the low-frequency peak ($St_u = 0.75$), the maximum levels for dipole and quadrupole noise are comparable, although the main radiation directions differ. The quadrupole sound is directed upstream primarily, where
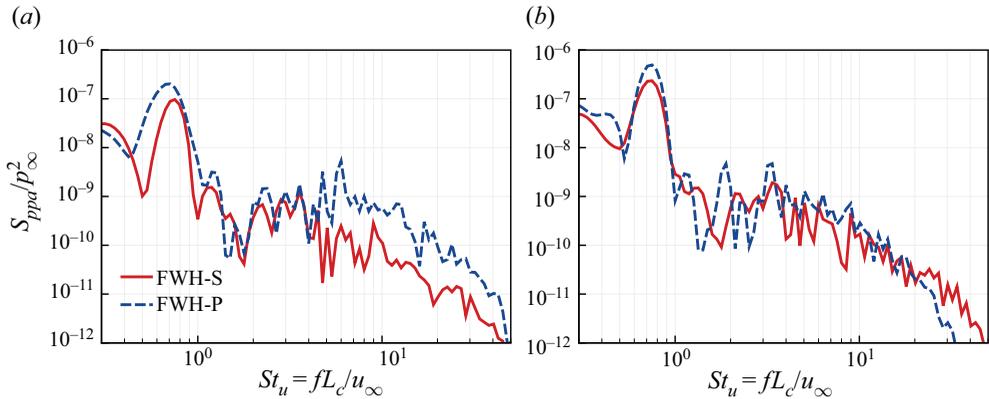
(*a*)

(*b*)

Figure 7. PSD functions of acoustic pressure (one-twelfth octave averaged) compared for FWH-S (p_D) and FWH-P (p_{Total}) predictions for $\alpha = 15°$. (*a*) $\theta = 90°$; (*b*) $\theta = 270°$.

the dipole sound is weakest. Consequently, the total noise radiation is less restricted towards the vertical directions than it is for the dipole-only component. At $St_u = 1.5$, the quadrupole sound increases relative to the dipole sound, becoming comparable or larger in every direction except directly below the aerofoil. Again, the largest quadrupole noise amplitude is radiated upstream, near $\theta = 150°$. For Strouhal numbers $St_u = 3.0, 6.0$ and 12.0, the quadrupole sound remains dominant. However, the largest sound amplitude is directed vertically, for $90° \le \theta \le 120°$. For $St_u = 24.0$, strong asymmetry is predicted by the FWH-P approach between the upper and lower half-planes. As mentioned previously, this could be due to blockage of the quadrupole sound on the suction side due to the body. This would be most significant for angles slightly upstream since the wake noise will also be blocked partially. Another possibility is a strong negative correlation between the dipole and quadrupole noise in this direction. A similar observation was also made by Spalart *et al.* (2019) for a noise source on one side of a fuselage.

The dominance of quadrupole sound in the upper half-plane is initially surprising considering the scaling laws of Curle ($p_Q^2 = O(M^8)$ and $p_D^2 = O(M^6)$), indicating $p_Q^2/p_D^2 \sim M^2$). However, an important consideration is that for separated flows, the relevant local Mach numbers for quadrupoles and dipoles might not be the same. For instance, the local convection speed near the TE (relevant for dipoles) is typically lower than the SSL convection speed (relevant for quadrupoles). On the contrary, for attached flow cases, the boundary layer convection speed is probably determinant for both sources of noise. A good estimate for p_Q/p_D may be attainable if the correct velocities can be calculated. However, this is not a straightforward task since there are likely multiple quadrupole sources occurring in different regions of the flow. To better demonstrate this, snapshots of the acoustic pressure field are shown at specific frequencies in figure 9. The bandpass filtered field is achieved with the equation

$$\left.\begin{array}{r}\widetilde{p}_a(\boldsymbol{x}, t) = \mathcal{F}^{-1}\{W(f)\, \mathcal{F}[p_a(\boldsymbol{x}, t)]\}, \\ W(f) = \exp[-\beta(f - f_p)^2/\Delta f^2] + \exp[-\beta(f + f_p)^2/\Delta f^2],\end{array}\right\} \quad (4.1)$$

where $\mathcal{F}$ and $\mathcal{F}^{-1}$ represent the Fourier and inverse Fourier transforms, respectively, and $W(f)$ is a narrow-band frequency filter with a bandwidth $\Delta f^* = 1$ at target frequency f_p. The coefficient $\beta = 20$ determines the steepness of the window function. The filtered
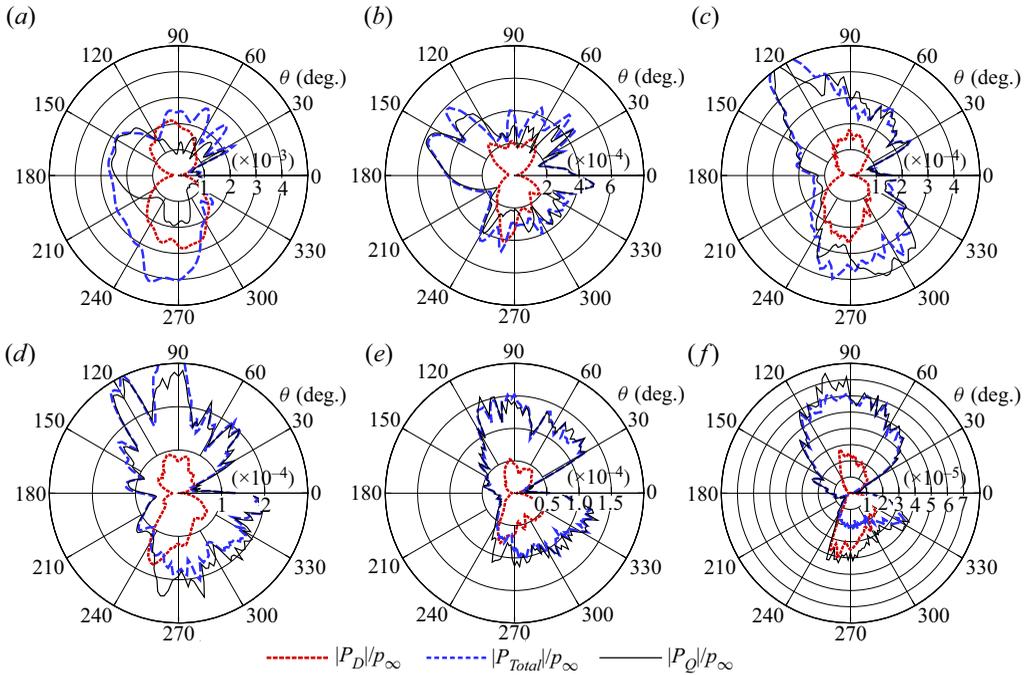
936 A34-12

Figure 8. One-third octave averaged sound directivity plots for $M_\infty = 0.4$ based on the magnitude of acoustic pressure Fourier transform (see (2.6)) at $R = 10L_c$ for (a) $St_u = 0.75$, (b) $St_u = 1.5$, (c) $St_u = 3.0$, (d) $St_u = 6.0$, (e) $St_u = 12.0$, and (f) $St_u = 24.0$.

pressure snapshots are shown at the end of the simulation. At low frequencies, $St_u = 0.75$ and 3.5, it is clear how sound waves are emitted directly from the near wake. This is a clear indication of low-frequency quadrupole sound (since the waves are not emitted from the aerofoil surface), hence the increase at low frequencies observed previously. At the von Kármán shedding frequency, the low-frequency wake noise is directed primarily upstream, which explains the strong upstream directivity for the quadrupole noise in figure 8(a). As the frequency is increased (see $St_u = 6.00$ and 10.00), interference patterns emerge, especially on the aerofoil suction side, indicating multiple noise sources. At high frequencies (see $St_u = 20.00$ and 40.00) it is clear how the separated shear layer directly above the aerofoil begins to play a more major role in the production of the noise.

The dominant flow features at the various frequencies are also identified by replotting with more appropriate contour levels. Figure 10 shows three-dimensional iso-surfaces of the filtered fluctuating pressure on the aerofoil suction side at four frequencies, $St_u = 0.75$, 3.5, 6.0 and 20.0. The sound waves are shown in the $z/L_c = -L_z/2$ and $y/L_c = 0$ planes. At $St_u = 0.75$, the dominating flow structure is the von Kármán vortex street. The highest intensity occurs in the near wake as indicated by the sound waves in figure 9(a). The structures are relatively uniform in the spanwise direction, which results in cylindrical sound propagation and minimal interference patterns. The filtered pressure field at $St_u = 3.50$ shows a combination of turbulent structures in the near wake, as well as spanwise-coherent vortices around one chord length downstream. The spanwise vortices likely play a meaningful role in the generation of the noise as indicated by the sound waves emitted from the wake in figure 9(b). At $St_u = 6.0$, vortices in the separated shear layer are highlighted in addition to small-scale structures near the TE and spanwise
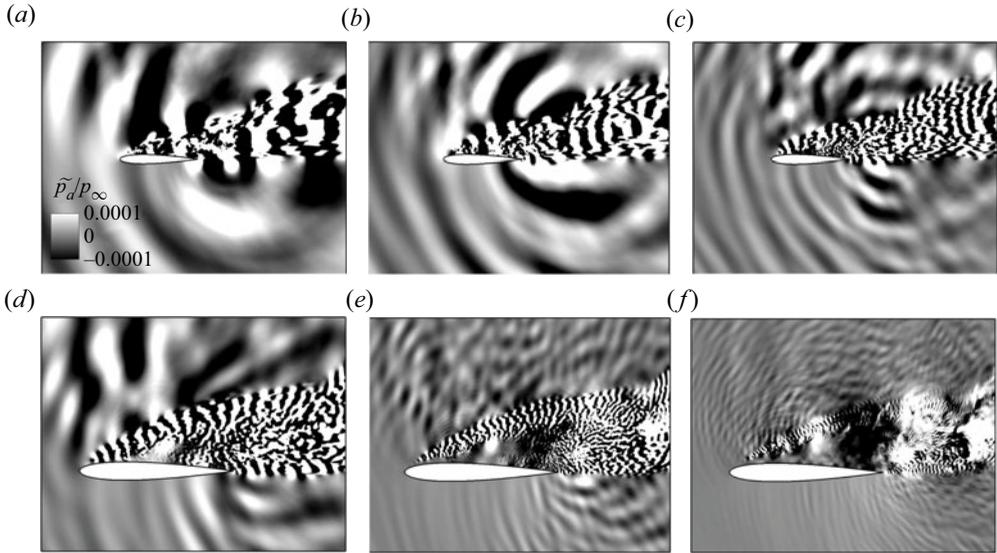
936 A34-13

(*a*)   (*b*)   (*c*)

$\widetilde{p}_a/p_\infty$
0.0001
0
−0.0001

(*d*)   (*e*)   (*f*)

Figure 9. Filtered fluctuating pressure field $\widetilde{p}_a$ obtained at the mid-span location for (*a*) $St_u = 0.75$, (*b*) $St_u = 3.50$, (*c*) $St_u = 6.00$, (*d*) $St_u = 10.00$, (*e*) $St_u = 20.00$, and (*f*) $St_u = 40.00$.

vortices in the wake. The multiple source regions lead to a more complex sound field with various interference effects. Similarly, at $St_u = 20.0$, Kelvin–Helmholtz vortices and the subsequent breakdown to turbulence also dominate the flow field along with small-scale structures near the TE. At high frequencies, it is also interesting to note that the sound field becomes more three-dimensional (as seen in the $y = 0$ plane) due to the breakdown of the dominating flow structures in the spanwise direction.

In figure 11(*a–d*) the spectral content at specific angles $\theta_0 = 120°$, $150°$, $210°$ and $250°$ is investigated more closely. The figure shows normalised sound power, calculated over $20°$ observer bands as in (2.8). Solutions based on p_{Total} (FWH-P), p_D (FWH-S) and p_Q are included. The figure provides further confirmation that the quadrupole sound is the larger of the two sources in the upper half-plane. At $\theta_0 = 120°$, the quadrupole noise is more than 10 dB greater than the dipole in the range $3 < St_u \leq 40$. Moving the observer further upstream tends to reduce the lower frequency bound where quadrupole noise begins to dominate. For $\theta_0 = 150°$, the quadrupole exceeds the dipole noise for the full frequency range by as much as 10 dB at low frequencies and 20 dB at high frequencies. The larger difference is due partly to significantly lower levels of dipole sound in the upstream/downstream directions. The low-frequency increase to the total noise due to quadrupoles differs from previously published results at low angles of attack where quadrupole contributions were limited to high frequencies (Wolf *et al.* 2012). As previously suggested, this is likely caused by radiation directly from the large-scale vortex shedding in the wake. For the equivalent upstream angle in the lower half-plane ($\theta_0 = 210°$), the quadrupole noise dominates a similar frequency range. However, the amplitude increase (relative to the dipole sound) is usually milder, between 0 and 5 dB. Comparatively, for $\theta_0 = 250°$, comparable amplitude levels are observed for both dipole and quadrupole results over most frequencies. When the amplitudes are similar, meaningful phase interactions are possible between the two sources. In this instance, constructive interference occurs for the low-frequency peaks when $St_u < 2$, while at high
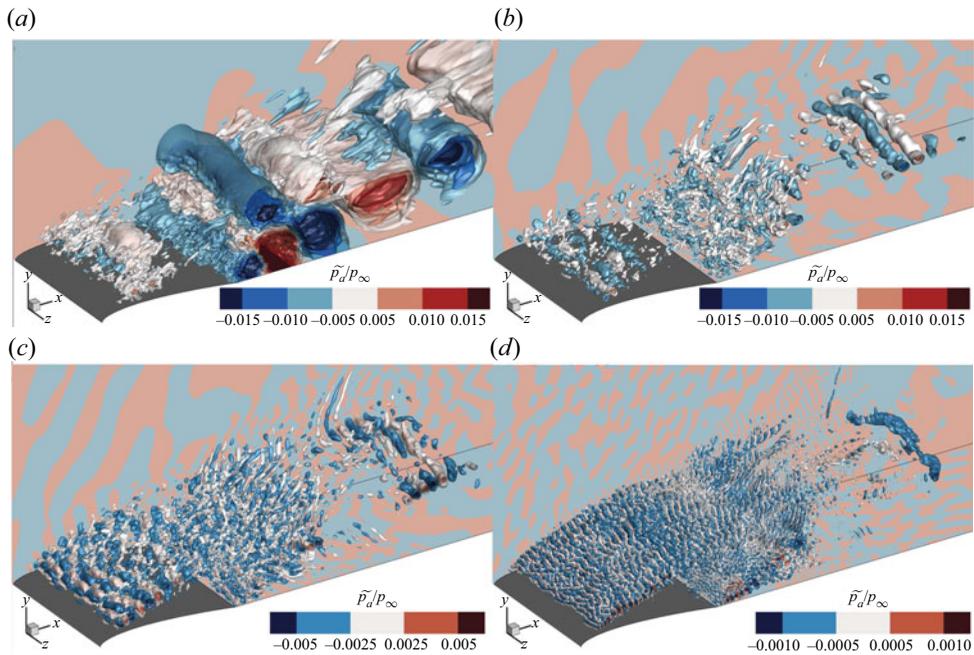
936 A34-14

Figure 10. Iso-surfaces of the filtered fluctuating pressure $\widetilde{p}_a$ shown on the aerofoil suction side: (*a*) $St_u = 0.75$, (*b*) $St_u = 3.50$, (*c*) $St_u = 6.00$, and (*d*) $St_u = 20.00$.

frequencies the two sources appear to interfere destructively, reducing the overall radiated noise.

5. Influence of Mach number on quadrupole noise

In this section, an additional simulation is carried out at the free-stream Mach number $M_\infty = 0.3$ to determine the effect of mean flow speed on the quadrupole noise. The aerofoil profile and angle of attack remain fixed. Figure 12 shows the sound fields obtained at the two flow speeds based on the divergence of velocity contours ($\boldsymbol{\nabla \cdot u}$). There is a visibly large difference between the two cases, with the $M_\infty = 0.3$ case demonstrating something closer to the more classical dipole sound radiation expected from a sharp TE aerofoil (although sound waves are also emitted from the SSL). At the higher Mach number, the quadrupole sources become qualitatively more significant. It is interesting to note how sound waves are generated from the wake for $M_\infty = 0.4$, which do not appear (visibly) for $M_\infty = 0.3$.

The radiated sound power (see (2.8)) produced by both solid and permeable FWH approaches is compared for the two Mach numbers in figures 13(*a,b*) for $\theta_0 = 90°$ and $\theta_0 = 120°$, respectively, versus St_a. The contribution from direct quadrupole sound remains significant for the lower Mach number case, although the increase in total noise begins at a slightly higher frequency compared to $M_\infty = 0.4$. This observation is consistent with the divergence field in figure 12, which clearly showed waves emitted from the large-scale structures in the wake in the higher Mach number case. The change in sound power level (PWL) spectra (increase in total noise due to the direct quadrupole contribution) can be calculated as

$$\Delta PWL_T = 10 \log_{10}(W_{Total}/W_D), \qquad (5.1)$$
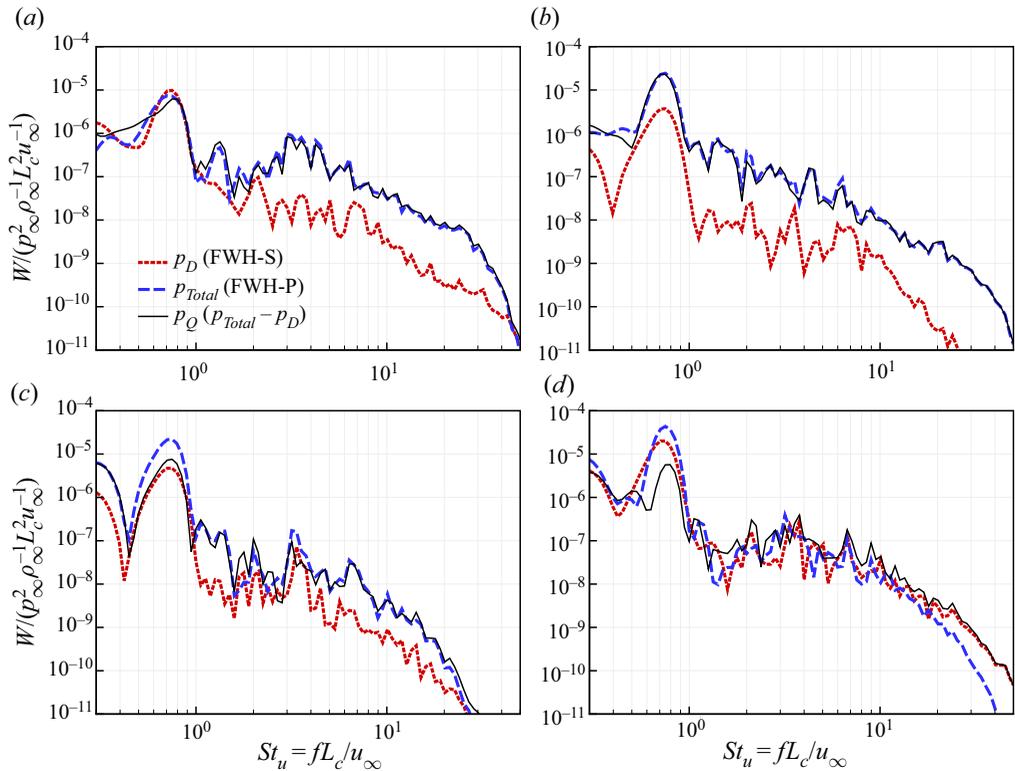
936 A34-15

Figure 11. Comparison of one-twelfth octave averaged normalised sound power predictions obtained based on p_D (FWH-S), p_{Total} (FWH-P) and p_Q ($p_{Total} - p_D$) for $\alpha = 15°$ at four observer angles: (*a*) $\theta_0 = 120°$, (*b*) $\theta_0 = 150°$, (*c*) $\theta_0 = 210°$, and (*d*) $\theta_0 = 250°$. Sound power is calculated over a $20°$ observer range.

where ΔPWL_T is plotted in figure 14 against the Strouhal number St_u. At $\theta_0 = 90°$, there is a fairly constant increase in total noise for $St_u \gtrsim 5.0$, with mean values 6.35 and 8.70 dB for $M_\infty = 0.3$ and 0.4, respectively. At $\theta_0 = 120°$, where the quadrupole sound tends to radiate more strongly (see figure 8), the noise increase rises significantly for the higher Mach number case.

Third octave directivity plots for $M_\infty = 0.3$ are shown in figures 15(*a–f*) for comparison with the higher Mach number case in figure 8. In figure 15, p_{Total} (FWH-S), p_D (FWH-P) and isolated p_Q sound predictions are shown at the Strouhal numbers $St_u = 0.75, 1.5, 3.0, 6.0, 12.0$ and 24.0. For the three highest frequencies, a similar trend is observed as for the $M_\infty = 0.4$ case. The largest radiated noise amplitude is in the upper half-plane close to $\theta = 120°$, with the quadrupole noise dominating there, and at other observer angles except around $240°$. At the lower three frequencies ($St_u = 0.75, 1.5, 3.0$), there is no clearly dominant radiation angle for the quadrupole sound. This differs from the results for $M_\infty = 0.4$, which showed strong radiation in the upstream direction for low frequencies. This difference could be due to the noise radiated from the downstream wake in the higher Mach number case. Figure 12 shows that a component of the wake noise radiates in the upstream direction. (This is most clear on the aerofoil underside where there is less interference from other sources.)

To approximate the Mach number scaling for dipoles and quadrupoles in the current simulations, we can consider the relative changes to p_D and p_Q. The Mach number scaling
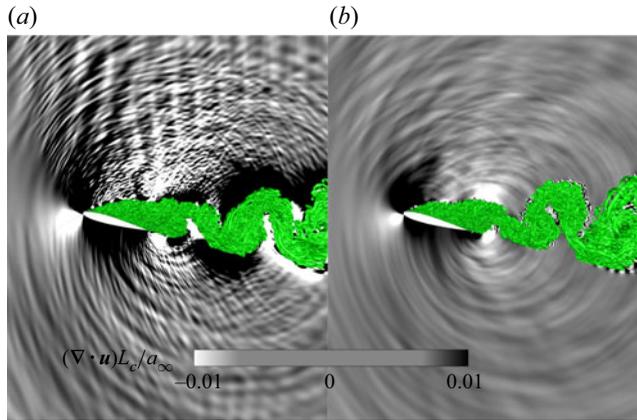
Figure 12. Normalised divergence of velocity contours $(\nabla \cdot \boldsymbol{u})L_c/a_\infty$ shown in the xy-plane at $z/L_c = 0$ for (a) $M_\infty = 0.4$ and (b) $M_\infty = 0.3$. The wake is visualised by the normalised Q-criterion ($QL_c^2/a_\infty^2 = 1.0$).

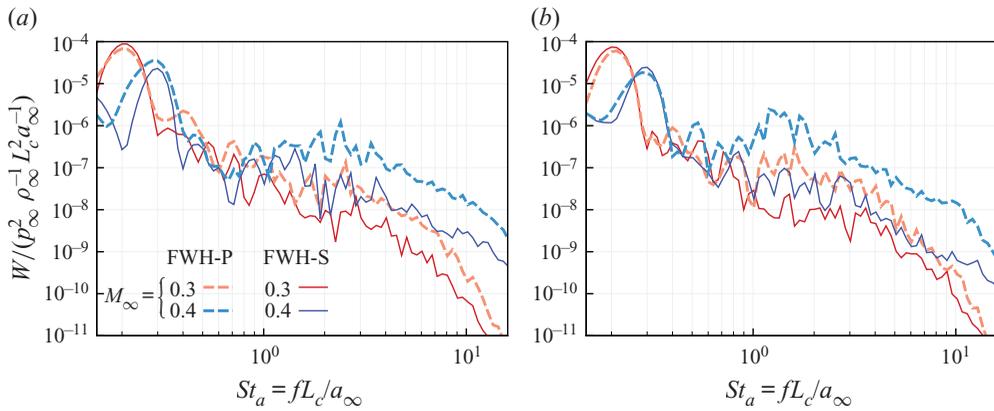Figure 13. One-twelfth octave averaged normalised sound power versus St_a obtained with the FWH-S (p_D) and FWH-P (p_{Total}) approaches at two Mach numbers, $M_\infty = 0.4$ and 0.3. (a) $\theta_0 = 90°$; (b) $\theta_0 = 120°$.
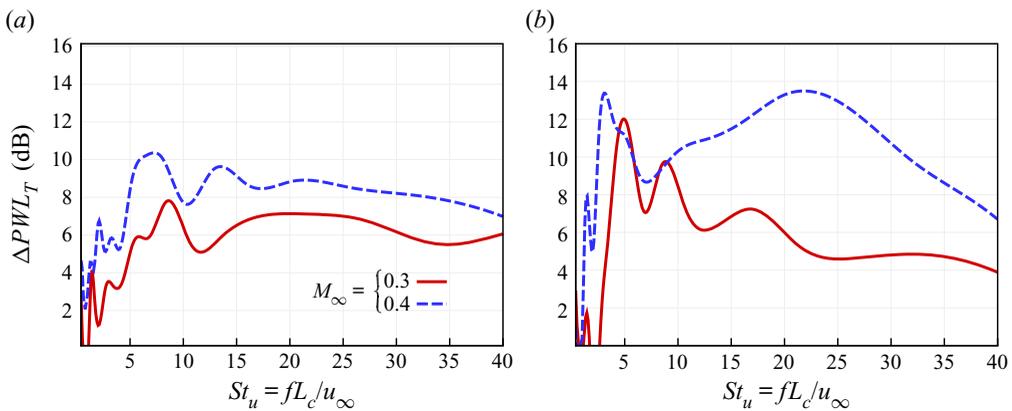

Figure 14. Increase in total noise due to quadrupole sources ΔPWL_T (calculated using one-third octave averaging). (a) $\theta_0 = 90°$; (b) $\theta_0 = 120°$.
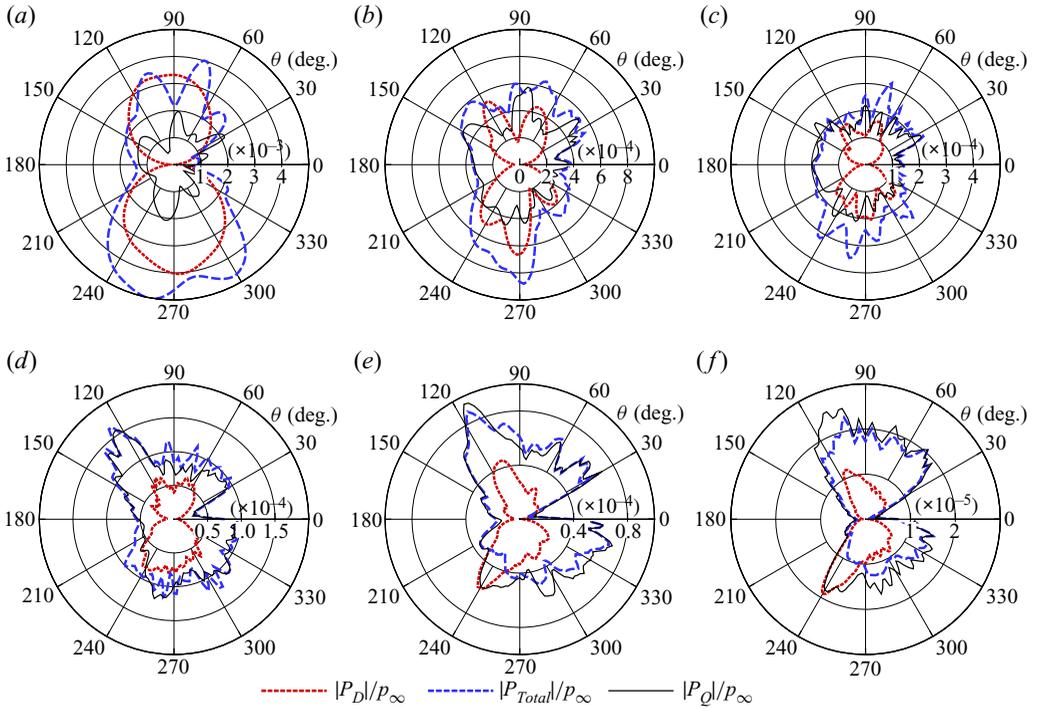
Figure 15. One-third octave averaged sound directivity plots for $M_\infty = 0.3$ based on the magnitude of acoustic pressure Fourier transform (see (2.6)) at $R = 10L_c$ for (a) $St_u = 0.75$, (b) $St_u = 1.5$, (c) $St_u = 3.0$, (d) $St_u = 6.0$, (e) $St_u = 12.0$, and (f) $St_u = 24.0$.

exponent can be determined by assuming a power-law relationship

$$\frac{W(St_a)|_{M_A}}{W(St_a)|_{M_B}} = \left(\frac{M_A}{M_B}\right)^{N_a}, \tag{5.2}$$

where W is the sound power spectra (2.8) based on St_a, calculated from either the dipole p_D or the quadrupole p_Q time signals. This rearranges to the following expression for N_a:

$$N_a = \frac{\log[W(St_a)|_{M_A}/W(St_a)|_{M_B}]}{\log(M_A/M_B)}. \tag{5.3}$$

An alternative expression for the scaling exponent can be obtained based on the power spectra as a function of St_u (rather than St_a), which provides

$$\frac{W(St_u)|_{M_A} \times M_A}{W(St_u)|_{M_B} \times M_B} = \left(\frac{M_A}{M_B}\right)^{N_u} \tag{5.4}$$

and

$$N_u = \frac{\log[W(St_u)|_{M_A}/W(St_u)|_{M_B}]}{\log(M_A/M_B)} + 1. \tag{5.5}$$

The factor M_A/M_B is included on the left-hand side of (5.4) due to the definition of the PSD as the power per unit frequency (in this case per unit St_u). The calculated values for N_u and N_a are shown in figure 16(a–h) at four observer angles, $\theta_0 = 60°$, $90°$, $120°$ and $150°$.
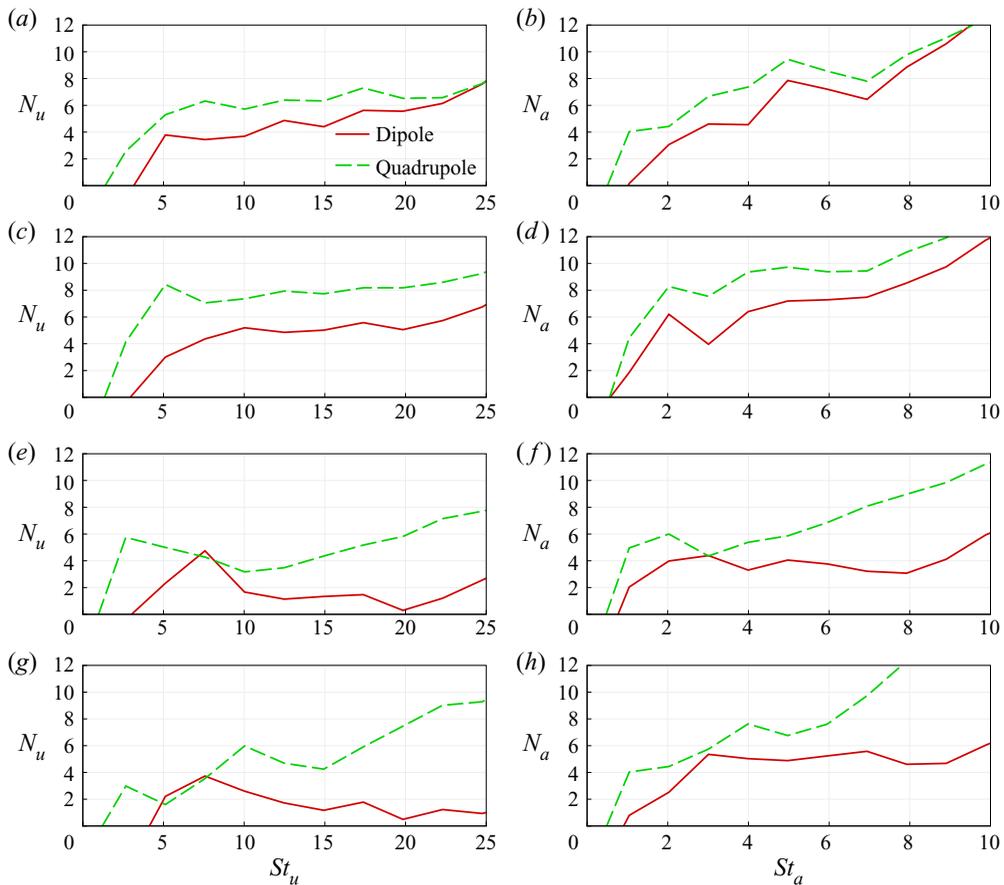
Figure 16. Mach number scaling exponents N_u and N_a due to increasing the Mach number from $M_\infty = 0.3$ to 0.4. The values of N_u (see (5.5)) and N_a (see (5.3)) are calculated as the difference in sound power spectra based on St_u and St_a, respectively (calculated using one-third octave averaging). (a,b) $\theta_0 = 60°$; (c,d) $\theta_0 = 90°$; (e,f) $\theta_0 = 120°$; (g,h) $\theta_0 = 150°$.

The outcome is non-trivial, with a strong dependence on frequency, frequency normalisation and observer angle. Consistent scaling against St_a may suggest that sound scattering plays a vital role in determining the radiated sound. Alternatively, more convincing results in plots versus St_u imply that coherent hydrodynamic features are important. It appears that the Mach number scaling based on St_u produces the most consistent trend (values of N_u) for the $\theta_0 = 60°$ and $90°$ observers regarding both dipole and quadrupole sources. At $\theta_0 = 60°$, the quadrupole noise oscillates around mean value $N_u = 6.5$ in the range $5 \leq St_u \leq 25$. This is close to the theoretical value $N_u = 7$ suggested by Spalart (2013) for quadrupoles in the presence of dipoles. At $\theta_0 = 90°$, the average value is $N_u = 8.1$ in the same range, close to the classical value $N = 8$. However, the dipole noise is close to the theoretical value of $N_u = 6$ only in a short range $15 \leq St_u \leq 22$. For $\theta_0 = 120°$ and $150°$, neither N_a nor N_u provides a consistent trend for the quadrupole noise scaling. On the other hand, for dipole sound, the N_a result is more convincing than that for N_u. The mean values of N_a in the range $2 \leq St_a \leq 10$ are $N_a = 4.0$ and 4.9, respectively, for $\theta_0 = 120°$ and $150°$. $N_a = 4.9$ is close to the value observed typically

for turbulent boundary layer scattering at a sharp TE, $N_a = 5$. One possible explanation for the rapidly increasing N values at high frequency is that the sound scaling based on the free-stream Mach number becomes less appropriate. The filtered flow field in figure 10 suggests that multiple flow regions are responsible for the noise at high frequencies. This includes Kelvin–Helmholtz vortices in the shear layer, turbulent flow near the TE, and spanwise wake vortices. Since all of these regions have different local flow speeds, it is difficult to determine the best value to use for the calculation of the sound scaling.

There are some similarities in the scaling exponent trends obtained for dipole and quadrupole sound, especially at $\theta_0 = 60°$ and $90°$. It is expected that the two sources are correlated, and therefore share some resemblance. However, the degree of similarity might indicate a more direct relationship between the dipole and quadrupole predictions. A possible explanation is identified by considering that the FWH-S approach contains a quadrupole sound component due to scattering by the aerofoil body. The current results suggest that the scattered quadrupole sound could be comparable or dominant to the dipole source radiation from the surface. Additionally, for $\theta_0 = 120°$ and $150°$, it is worth noting that the dipole noise scales closer to the theoretical value when the scaling exponent is calculated based on St_a. This could also be an indication of significant sound scattering phenomena. This is supported by figure 10, which shows the dominant flow structures for mid-to-high frequencies away from the wall (or aft of the TE), indicating that TE scattering may not be significant. Another indication of this was provided in the previous paper by the authors (Turner & Kim 2020a). It was shown that for the mid-to-high frequencies, the wall pressure fluctuations were both weaker and had reduced chordwise phase variation compared to lower angles of attack, possibly indicating acoustics pressure disturbances.

6. Influence of incidence angle on quadrupole noise

In this section, the full-stall case is compared to pre-stall ($\alpha = 5°$) and near-stall ($\alpha = 10°$) conditions. The two additional datasets are carried out based on $M_\infty = 0.4$ with $L_z = 0.2L_c$ for the pre-stall case, and $L_z = L_c$ for the near-stall case (Turner & Kim 2020a). Figure 17 compares the divergence of velocity and local Mach number fields for the three incidence angles. At the lowest incidence angle, there is a laminar separation bubble around the mid-chord location. Upon reattachment, the flow transitions to turbulence, remaining attached until the TE point. Increasing the angle of attack causes the separation bubble to shift towards the LE. At $\alpha = 10°$, the aerofoil is near the maximum lift condition. There is a short bubble near the LE and a turbulent boundary layer over the majority of the suction surface. Some separation is also observed near the TE intermittently. Above this angle, the bubble bursts, leading to the full stall condition seen previously in this paper.

The sound field produced by the pre-stall case radiates primarily from the TE, except for some sound waves from the transition/reattachment region (possibly due to quadrupole sources appearing there). On the other hand, the near- and full-stall cases seem to radiate noise mainly from the SSL and downstream wakes. It is evident from the divergence fields that the noise produced at higher angles of attack also contains increased amplitude high-frequency waves. This is an expected outcome since the transition occurs further upstream at higher incidence angles. Another factor is the increased flow velocity near the transition point. For example, the $\alpha = 10°$ case experiences transition and reattachment of the laminar separation bubble within the first quarter chord, whereas the transition occurs around the mid-chord in the pre-stall condition where the local Mach number is lower. The instantaneous snapshots of the local Mach number field in figure 17 show higher and more consistent values along the edge of the SSL for the near-stall case compared to full-stall.

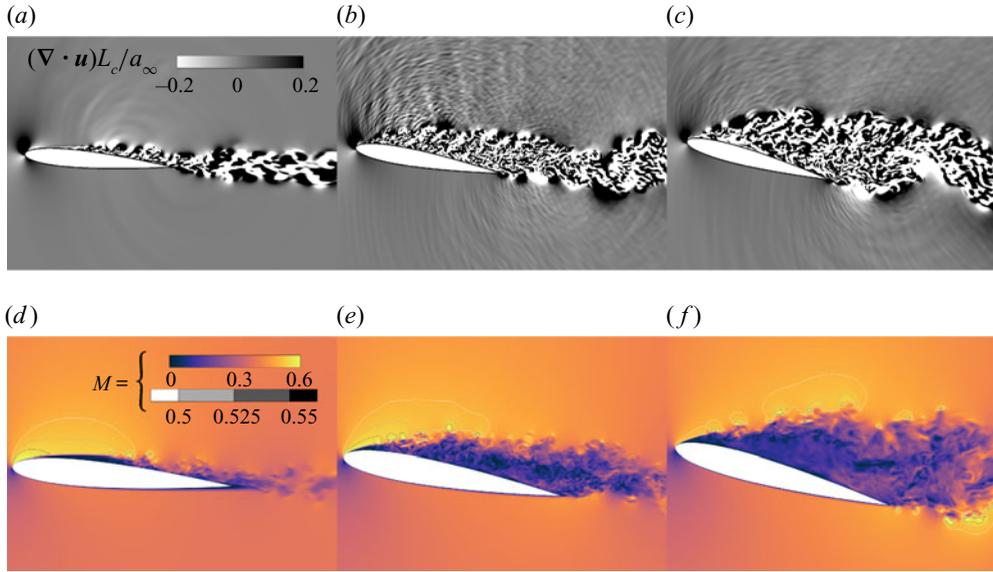(*a*)　　　　　　　　　　(*b*)　　　　　　　　　　(*c*)

(*d*)　　　　　　　　　　(*e*)　　　　　　　　　　(*f*)

Figure 17. (*a–c*) Instantaneous divergence of velocity fields produced at the mid-span location for the three angles of attack $\alpha = 5°$, $\alpha = 10°$ and $\alpha = 15°$. (*d–f*) Local Mach number fields. Specific contour bands $M = 0.5$, 0.525 and 0.55 shown in greyscale.

Conversely, the full-stall case has higher Mach number values directly downstream of the TE, possibly indicating stronger quadrupole noise from the eddies generated there.

Figure 18 shows the radiated power spectra predicted by FWH-S (p_D) and FWH-P (p_{Total}) at the three angles of attack. The dipole results predicted by FWH-S have been discussed in detail in the previous paper by the authors (Turner & Kim 2020*a*). Here they are repeated in order to analyse the trend changes when quadrupole sources are also included. The dipole noise can be separated into three frequency bands where different behaviours are observed. At low frequencies, increased broadband noise is observed for the near- and full-stall cases, with additional broad peaks due to wake shedding. At medium frequencies, the results are more similar for all angles of attack. Finally, at high frequencies, the near-stall case dominates. If the quadrupole sources are accounted for, then the trend changes due to increased overall noise levels for the full-stall case. More specifically, at high frequencies, the gap between near-stall and full-stall is significantly reduced, while at low frequencies, the full-stall case becomes more dominant. The total noise increase due to the direct quadrupole contribution is quantified in figures 19(*a–d*) for $\theta_0 = 60°$, $90°$, $120°$ and $150°$ at the three angles of attack. The increase in total noise due to quadrupole sound is shown to increase with the incidence angle. For $\alpha = 5°$, the noise increase is typically below 5 dB, which provides some confirmation of the results as this is consistent with the findings of Wolf *et al.* (2012) at the same angle of attack but higher Reynolds number. In the near-stall condition ($\alpha = 10°$), ΔPWL_T is increased most for upstream angles, particularly high frequencies. This is likely caused by the higher velocity turbulent SSL on the aerofoil suction side, discussed previously. For the full-stall case ($\alpha = 15°$), ΔPWL_T is increased further: mildly in the vertical direction, and more significantly upstream and downstream. The largest increase in ΔPWL_T during full-stall relative to the near-stall case occurs at $\theta = 150°$ for $St_u > 20$.

The increased ΔPWL_T values in full-stall at high frequencies are interesting since the isolated quadrupole sound level is actually lower than in the near-stall case. This is
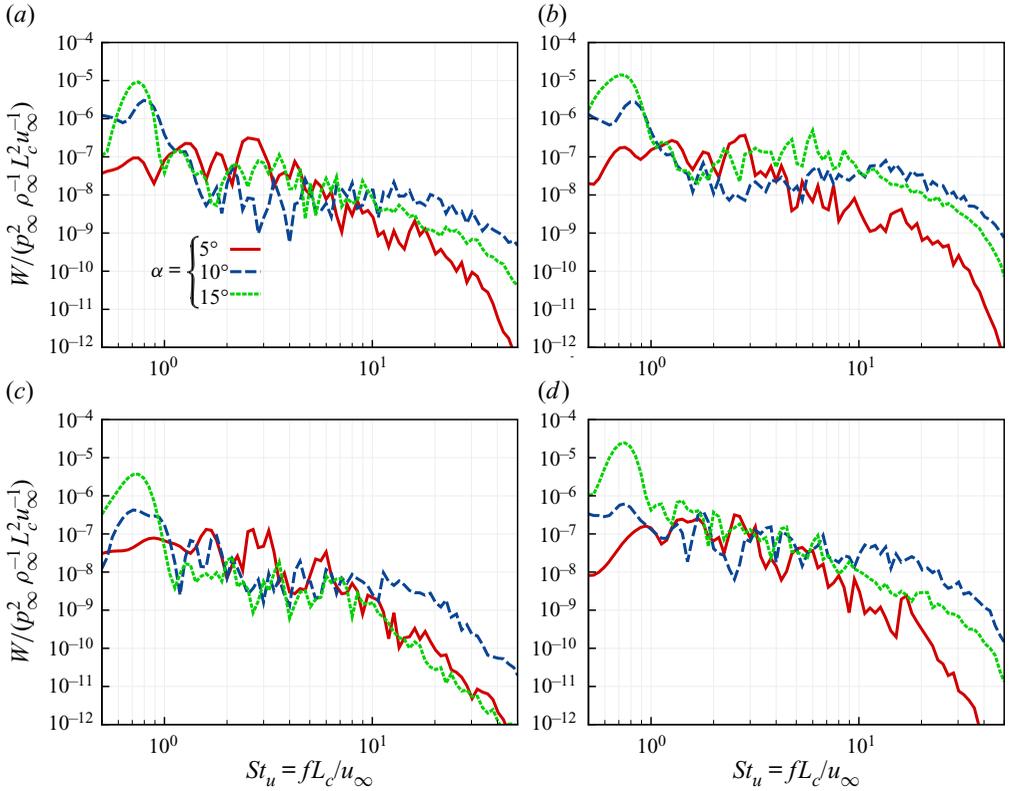
(*a*)

(*b*)

(*c*)

(*d*)

Figure 18. Comparison of the one-twelfth octave averaged normalised sound power obtained for the three angles of attack by using both the FWH-S (p_D) and FWH-P (p_{Total}) approaches. (*a*) FWH-S, $\theta_0 = 90°$; (*b*) FWH-P, $\theta_0 = 90°$; (*c*) FWH-S, $\theta_0 = 150°$; (*d*) FWH-P, $\theta_0 = 150°$.
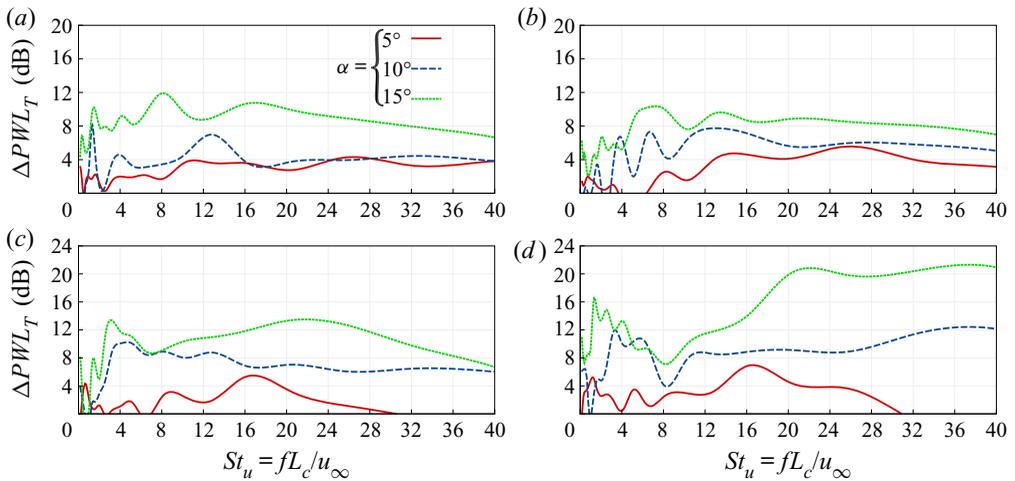
(*a*)

(*b*)

(*c*)

(*d*)

Figure 19. Increase in total noise due to quadrupole sources ΔPWL_T at the three angles of attack (calculated using one-third octave averaging): (*a*) $\theta_0 = 60°$, (*b*) $\theta_0 = 90°$, (*c*) $\theta_0 = 120°$, and (*d*) $\theta_0 = 150°$.
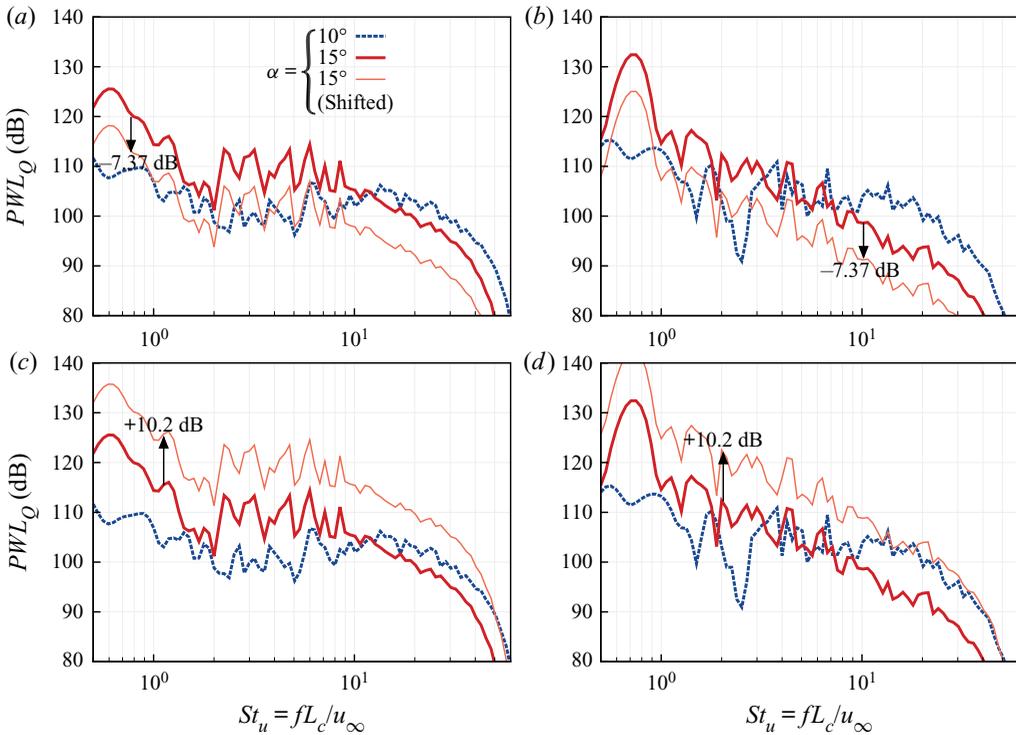
Figure 20. One-twelfth octave averaged sound power level based on p_Q compared for the near-stall ($\alpha = 10°$) and full-stall (15°) cases. The full-stall result is also shown scaled by $\Delta PWL_{SSL} = 10.2$ dB and $\Delta PWL_{Wake} = -7.37$ dB, calculated via (6.1) and (6.2), respectively. (*a,b*) -7.37 dB shift compared at $\theta_0 = 90°$ and $150°$. (*c,d*) $+10.2$ dB shift compared at $\theta_0 = 90°$ and $150°$. Reference power $W_{Ref}/(p_\infty^2 \rho_\infty^{-1} L_c^2 a_\infty^{-1}) = 3.3 \times 10^{-18}$.

verified in figure 20, which compares the quadrupole sound power level (PWL_Q) based on p_Q for the two angles of attack at $\theta_0 = 90°$ and $150°$. The increased significance of quadrupole noise at high frequencies during full-stall is therefore not caused purely by increased quadrupole noise generation. Also, it is caused by weaker dipole sound relative to the quadrupole sound, when compared with the near-stall condition. For $\alpha = 10°$, the small-scale structures in the SSL remain close to the wall. Therefore they can induce a significant unsteady pressure footprint near the TE. On the other hand, in full-stall, the distance between the aerofoil and the SSL means that there is a reduced pressure footprint. For this reason, the high-frequency dipole noise is lower (see figure 18), meaning that quadrupole sound directly from the turbulence represents a larger proportion of the radiated noise. The situation is very different at low frequencies, where the broadband dipole sound is more comparable for near- and full-stall; however, the quadrupole sound is greater in full-stall – see figure 20.

To infer more understanding of the quadrupole sound generation mechanisms, PWL_Q can be scaled relative to local Mach number variations in the SSL and wake. Figure 21 shows the time-averaged Mach numbers for $\alpha = 10°$ and $15°$, respectively, for the LE–SSL and downstream wake regions. The maximum mean Mach number for the LE–SSL region ($x/L_c < 0$) is $\max[\overline{M_{SSL}}] = 0.751$ for $\alpha = 10°$ versus $\max[\overline{M_{SSL}}] = 0.560$ for $\alpha = 15°$, whereas in the wake ($x/L_c > 0.5$), $\max[\overline{M_{Wake}}] = 0.406$ versus 0.502. Based on these

936 A34-23
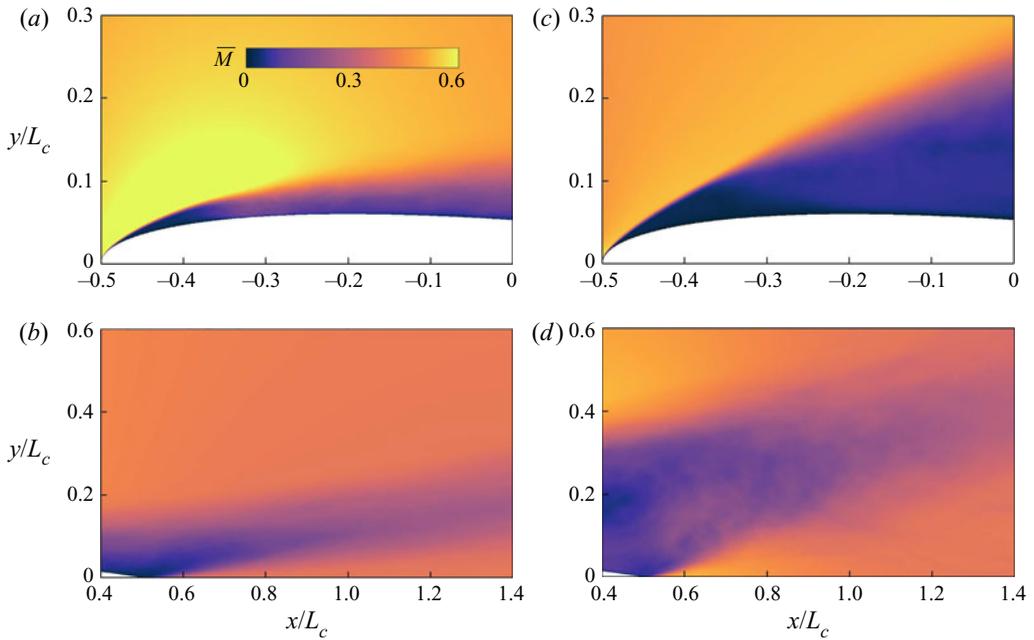
Figure 21. Time-averaged local Mach number for the LE–SSL and wake regions. (*a,b*) $\alpha = 10°$; (*c,d*) $\alpha = 15°$.

values, the spectra in figure 20 are scaled by the following factors:

$$\Delta PWL_{SSL} = 10 \log_{10} \left[\left(\frac{\max[\overline{M_{SSL}}]|_{\alpha=10°}}{\max[\overline{M_{SSL}}]|_{\alpha=15°}} \right)^{N_u} \right], \tag{6.1}$$

$$\Delta PWL_{Wake} = 10 \log_{10} \left[\left(\frac{\max[\overline{M_{Wake}}]|_{\alpha=10°}}{\max[\overline{M_{Wake}}]|_{\alpha=15°}} \right)^{N_u} \right]. \tag{6.2}$$

Assuming a power of eight scaling ($N_u = 8$) results in a vertical shift of $\Delta PWL_{SSL} = +10.2$ dB and $\Delta PWL_{Wake} = -7.37$ dB applied to the $\alpha = 15°$ result. The rescaled spectra are plotted in figure 20, and show good agreement with the near-stall case at high and low frequencies, respectively. This helps to confirm that the high level of high-frequency sound for near-stall conditions is due to higher local flow speed in the LE–SSL. Similarly, the increased low-frequency broadband quadrupole sound during full-stall is likely linked to the velocity in the wake. In the previous section, it was observed that the free-stream Mach number scaling exponent depends on the frequency. The current result suggests an alternative, that the relevant Mach number used to scale the spectra could vary with frequency (depending on the source region) while the exponent remains fixed.

7. Conclusions

Direct numerical simulations of an NACA0012 aerofoil at $Re_\infty = 50\,000$ were carried out to determine the importance of quadrupole noise during aerofoil flow separation or stall conditions. For a free-stream Mach number $M_\infty = 0.4$ and $\alpha = 15°$ angle of attack, quadrupole noise was dominant for a wide range of frequencies (depending on the

observer angle). For low frequencies, the quadrupole noise radiated mainly upstream, whereas for mid-to-high frequency ($St_u > 3.0$), it was strongest for $90° \leq \theta \leq 120°$. The largest differences between the quadrupole and dipole noise are found in the upper half-plane, which was consistent with the separation and transition occurring only on the aerofoil suction side under the chosen flow conditions. A bandpass filtering approach was used to visualise the sound waves and flow structures at various frequencies. This revealed multiple source regions for the quadrupole sound, depending on the frequency. At low frequencies, the sound is primarily emitted from coherent wake vortices, while at higher frequencies, turbulence flow near the TE and Kelvin–Helmholtz vortices also contribute.

A detailed discussion of the Mach number scaling has been given at $M_\infty = 0.3$ and 0.4. The total radiated sound power (integrated over all observers) was increased by several decibels for both Mach number cases, most predominantly for $St_u \approx 5 - 15$. It was found that the Mach number scaling exponent deviated significantly from the classical values of 6 for dipoles and 8 for quadrupoles, varying with the observer angle, frequency range and frequency normalisation ($St_u = fL_c/u_\infty$ or $St_a = fL_c/a_\infty$). The scaling exponent based on St_u appeared to work best for the quadrupole sound at vertical and downstream angles, whereas the dipole sound scaled more consistently when the exponent was calculated based on St_a in the upstream directions. This may indicate that a large portion of the 'dipole' sound estimated by FWH-S could be related to the surface scattering of pre-generated quadrupole sound, rather than the genuine dipole sound generated from the surface. This may need further investigations in the future.

Two additional angles of attack were also investigated at $M_\infty = 0.4$: pre-stall $\alpha = 5°$, and near-stall $\alpha = 10°$. Relatively, the full-stall case produced the most quadrupole sound for low-to-mid frequencies ($St_u \lesssim 10$), and the near-stall case for the high frequencies. Despite this, the quadrupole represented a larger proportion of the total radiated noise for the full stall case at all frequencies. Evidence for a link between the radiated quadrupole sound and the maximum mean Mach number in the LE separated shear layer and wake regions was also presented.

The current study makes a meaningful step towards quantifying and explaining the composition of aerofoil noise in flow separation or stall conditions. Despite this, there is still a vast parameter space to explore to fully understand aerofoil stall noise. One area of interest is flow separation from the TE (instead of from the LE as investigated in this paper), which occurs for thicker aerofoils or higher Reynolds number flows.

Author ORCIDs.
Jacob M. Turner https://orcid.org/0000-0002-0522-4340;
Jae Wook Kim https://orcid.org/0000-0003-0476-2574.

(*a*) (*b*)
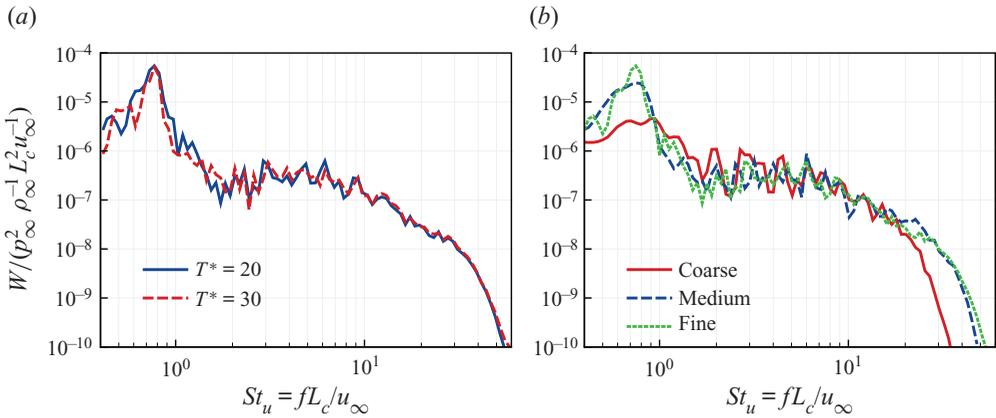

Figure 22. One-twelfth octave averaged sound power at $\theta_0 = 90°$. (*a*) Comparison between the default ($Ta_\infty/L_c = 20$) and extended ($Ta_\infty/L_c = 30$) time signals. (*b*) Comparison for three grid levels.

	N_ξ	N_η	N_ζ
Coarse	600	560	163
Medium	900	840	245
Fine	1200	1120	326

Table 1. Grid levels used for the grid convergence study shown in figure 22(*b*).

Appendix. Spectra convergence

In this appendix, the sensitivity of the spectra is investigated in more detail. First, the DNS for $\alpha = 15°$ and $M_\infty = 0.4$ is run for an additional 10 time units to determine if the signal lengths are long enough for statistical convergence. Figure 22(*a*) compares the one-twelfth octave averaged sound power at $\theta_0 = 90°$ calculated with the original and extended time signals. Overall, good agreement is achieved, with only minor differences at low frequencies. This verifies that the default sample period is sufficient to capture the key features in the spectra (including the von Kármán peak shedding frequency).

Figure 22(*b*) shows the influence of grid resolution on the predicted far-field noise obtained with the FWH-P approach. The DNS results are compared with predictions made with two coarser implicit large-eddy simulations. Details of the three grids are provided in table 1. The coarsest grid fails to predict the von Kármán shedding peak at $St_u = 0.75$. Additionally, there is significant attenuation of the high frequencies occurring above $St_u > 20$. Despite this, the far-field spectra converge convincingly when the grid is refined. The medium and fine grid levels show good agreement for most of the frequency range, especially mid-to-high frequencies. The largest differences occur at low frequency. The shedding peak is broadened by the coarser grid level. This is an expected outcome caused by increased dispersion of the wake vortices (which are important for the prediction of the low-frequency quadrupole noise).

REFERENCES

BERTAGNOLIO, F., AAGAARD MADSEN, H., FISCHER, A. & BAK, C. 2015 Experimental characterization of stall noise toward its modelling. In *Proceedings of the 6th International Conference on Wind Turbine Noise*. Glasgow, UK.

BROOKS, T.F., POPE, D.S. & MARCOLINI, M.A. 1953 Airfoil self-noise and prediction. NASA reference publication 1218.

CURLE, N. 1955 The influence of solid boundaries upon aerodynamics sound. *Proc. R. Soc. Lond.* A **231**, 505–514.

DI FRANCESCANTONIO, P. 1997 A new boundary integral formulation for the prediction of sound radiation. *J. Sound Vib.* **202**, 491–509.

FARASSAT, F. & SUCCI, G.P. 1980 A review of propeller discrete frequency noise prediction technology with emphasis on two current methods for time domain calculations. *J. Sound Vib.* **71**, 399–419.

FFOWCS WILLIAMS, J.E. & HAWKINGS, D.L. 1969 Sound generation by turbulence and surface in arbitrary motion. *Philos. Trans. R. Soc. Lond.* A **264**, 321–342.

FINK, M.R. & BAILEY, D.A. 1980 Airframe noise reduction studies and clean-airframe noise investigation. NASA CR-159311.

GARRICK, I.E. & WATKINS, C.E. 1953 A theoretical study of the effect of forward speed on the free-space sound-pressure field around propellers. NACA TN-3018.

GEORGIADIS, N.J., RIZZETTA, D.P. & FUREBY, C. 2010 Large-eddy simulations: current capabilities recommended practices, and future research. *AIAA J.* **48** (8), 1772–1784.

GOLDSTEIN, M.E. 1976 *Aeroacoustics*. McGraw-Hill.

KIM, J.W. 2007 Optimised boundary compact finite difference schemes for computational aeroacoustics. *J. Comput. Phys.* **225**, 995–1019.

KIM, J.W. 2010 High-order compact filters with variable cut-off wavenumber and stable boundary treatment. *Comput. Fluids* **39**, 1168–1182.

KIM, J.W. 2013 Quasi-disjoint pentadiagonal matrix systems for the parallelization of compact finite-difference schemes and filters. *J. Comput. Phys.* **241**, 168–194.

KIM, J.W., LAU, A.S.H. & SANDHAM, N.D. 2010a CAA boundary conditions for airfoil noise due to high-frequency gusts. *Proc. Engng* **6**, 244–253.

KIM, J.W., LAU, A.S.H. & SANDHAM, N.D. 2010b Proposed boundary conditions for gust-airfoil interaction noise. *AIAA J.* **48** (11), 2705–2709.

KIM, J.W. & LEE, D.J. 2000 Generalized characteristic boundary conditions for computational aeroacoustics. *AIAA J.* **38** (11), 2040–2049.

KIM, J.W. & LEE, D.J. 2004 Generalized characteristic boundary conditions for computational aeroacoustics, part 2. *AIAA J.* **42** (1), 47–55.

KIM, J.W. & MORRIS, P.J. 2002 Computation of subsonic inviscid flow past a cone using high-order schemes. *AIAA J.* **40** (10), 1961–1968.

LACAGNINA, G., et al. 2019 Mechanisms of airfoil noise near stall conditions. *Phys. Rev. Fluids* **4**, 123902.

LARATRO, A., ARJOMANDI, M., CAZZOLATO, B. & KELSO, R. 2017 Self-noise of NACA0012 and NACA0021 aerofoils at the onset of stall. *Intl J. Aeroacoust.* **16** (3), 181–195.

MAYER, Y.D., ZANG, B. & AZARPEYVAND, M. 2019 Aeroacoustic characteristics of a NACA 0012 airfoil for attached and stalled flow conditions. In *25th AIAA/CEAS Aeroacoustics Conference*. AIAA Paper 2019-2530.

MOREAU, S., ROGER, M. & CHRISTOPHE, J. 2009 Flow features and self-noise of airfoils near stall or in stall. In *15th AIAA/CEAS Aeroacoustics Conference*. AIAA Paper 2009-3198.

PATERSON, R.W., AMIET, R.K. & LEE MUNCH, C. 1975 Isolated airfoil-tip vortex interaction noise. *J. Aircraft* **12** (1), 34–40.

SHUR, M.L., SPALART, P.R. & STRELETS, M.K.. 2005 Noise prediction for increasingly complex jets. Part 1: methods and tests. *Intl J. Aeroacoust.* **4**, 213–246.

SPALART, P.R. 2013 On the precise implications of acoustic analogies for aerodynamic noise at low Mach numbers. *J. Sound Vib.* **332**, 2808–2815.

SPALART, P.R., BELYAEV, K.V., SHUR, M.K., STRELETS, M.K.. & TRAVIN, A.K. 2019 On the differences in noise predictions based on solid and permeable Ffowcs Williams-Hawkings integral solutions. *Intl J. Aeroacoust.* **18**, 621–646.

TURNER, J.M. & KIM, J.W. 2020a Aerofoil dipole noise due to flow separation and stall at a low Reynolds number. *Intl J. Heat Fluid Flow* **86**, 108715.

TURNER, J.M. & KIM, J.W. 2020b Effect of spanwise domain size on direct numerical simulations of airfoil noise during flow separation and stall. *Phys. Fluids* **32**, 065103.

WHITE, F.M. 1991 *Viscous Fluid Flow*. McGraw-Hill.

WOLF, W.R., AZEVEDO, J.L.F. & LELE, S.K. 2012 Convective effects and the role of quadrupole sources for aerofoil aeroacoustics. *J. Fluid Mech.* **708**, 502–538.

ZANG, B., MAYER, Y.D. & AZARPEYVAND, M. 2020 On the aerodynamic and aeroacoustic characteristics of a NACA 65-410 airfoil at moderate Reynolds number. *AIAA Paper* 2020-2599. AIAA Aviation 2020 Forum.